

# Communication-Efficient Distributed Inverse Quantum Fourier Transform

F. Javier Cardama<sup>a</sup>, Jorge Vázquez-Pérez<sup>c</sup>, Tomás F. Pena<sup>a,b</sup>, Andrés Gómez<sup>c</sup>

<sup>a</sup>Centro Singular de Investigación en Tecnoloxías Intelixentes (CITIUS), Universidade de Santiago de Compostela, Santiago de Compostela, 15782, Spain

<sup>b</sup>Departamento de Electrónica e Computación, Universidade de Santiago de Compostela, Santiago de Compostela, 15782, Spain

<sup>c</sup>Galicia Supercomputing Center (CESGA), Avda. de Vigo S/N, Santiago de Compostela, 15705, Spain

---

## Abstract

The scalability of quantum computing is currently limited by physical, technological, and architectural constraints that hinder the integration of a large number of qubits within a single quantum processor. Distributed quantum computing (DQC) has therefore emerged as a viable alternative, aiming to interconnect multiple smaller quantum processing units (QPUs) to jointly operate on a global quantum state. While this paradigm enables scalable architectures, it introduces significant communication overhead due to the cost of non-local quantum operations across distant nodes. In this work we propose a distributed formulation of the iQFT over a quantum network composed of  $P$  nodes, each hosting  $Q$  qubits, enabling the execution on a logical register of size  $n = P \cdot Q$ . Furthermore, we introduce a communication-efficient variant based on a threshold-driven pruning strategy, referred to as a *communication horizon*, which exploits the exponentially decreasing significance of controlled-phase rotations to safely omit remote gates with negligible impact. By reducing the number of inter-node quantum interactions, the proposed approach significantly lowers the quantum communication requirements of the distributed iQFT while preserving its functional correctness. Crucially, we show that this approach fundamentally alters the scaling of the algorithm: the entanglement resource consumption per node saturates to a constant value, reducing the global communication complexity from quadratic  $O(P^2)$  to linear  $O(P)$ . As the iQFT constitutes a critical building block in many quantum algorithms, the techniques presented in this paper directly contribute to improving the practicality and scalability of distributed quantum computation.

*Keywords:* distributed quantum computing, quantum fourier transform, quantum algorithms, quantum communication.

---

## 1. Introduction

Distributed quantum computing (DQC) has emerged as a promising architectural approach to overcome the scalability limitations of current monolithic quantum processors [1, 2], which are fundamentally constrained by qubit noise, decoherence, and the increasing complexity of control and calibration as the system size grows [3, 4, 5]. Rather than relying on a single large quantum processor, DQC interconnects multiple smaller quantum processing units (QPUs) through quantum entanglement and classical communication channels, enabling the creation of a global quantum state spanning several physical devices [6, 7, 8]. By entangling qubits across a network of  $P$  interconnected QPUs, each hosting  $Q$  local qubits, a collective logical register of size  $n = P \cdot Q$  can be realized. This modular paradigm allows quantum systems to scale beyond the physical limits of individual processors [9, 10].

Regarding quantum computing itself, it represents a fundamental shift in the computational paradigm, with several cornerstone quantum algorithms demonstrating its advantage, being the well known Shor's integer factorization algorithm [11] the most representative. Shor's algorithm leverages the Quantum Phase Estimation (QPE) [12] algorithm to factor large integers in polynomial time, with the inverse Quantum Fourier Transform (iQFT) playing a central role in it, due to the QPE encoding its final results in the relative phases of quantum states expressed in the Fourier basis. The iQFT acts as a decoding

operation that transforms this phase information back into the computational basis, enabling the extraction of classical outcomes through measurement. Consequently, the efficiency and scalability of the iQFT directly impact the performance of the QPE and, therefore, the Shor's algorithm—and all of those employing these oracle as part of their operations.

However, the standard implementation of the iQFT on an  $n$ -qubit register requires  $O(n^2)$  two-qubit controlled-phase gates and exhibits an all-to-all interaction pattern, as each qubit must, in principle, interact with every other qubit. This quadratic gate complexity and dense connectivity pose significant challenges for both monolithic and distributed quantum architectures. In distributed settings, the cost of non-local two-qubit gates is particularly high, as they require entanglement generation, quantum communication, and classical synchronization between remote nodes [13, 14, 15].

In this work, we address these challenges by proposing a communication-efficient distributed implementation of the iQFT. The main contributions of this paper are twofold:

- **Distributed iQFT:** we present a systematic decomposition of the iQFT across a quantum network composed of  $P$  nodes, each with  $Q$  qubits, enabling the execution of the transform over a global register of size  $n = P \cdot Q$ .
- **Communication-efficient:** we introduce a communication optimized variant of the distributed iQFT based on a

well-known threshold-driven pruning strategy [16].

The remainder of this paper is organized as follows. Section 2 reviews the theoretical background of the iQFT and distributed quantum computing primitives. Section 3 introduces the proposed distributed iQFT formulation and the communication horizon optimization strategy. Section 4 analyzes the impact of the proposed approach in terms of communication cost and accuracy. Finally, Section 5 and 6 conclude the paper and outlines directions for future research.

## 2. Background

### 2.1. Inverse Quantum Fourier Transform

The Quantum Fourier Transform (QFT) is a linear unitary transformation analogous to the classical discrete Fourier transform. For a quantum system of  $n$  qubits, let  $N = 2^n$  be the dimension of the Hilbert space. The QFT maps the orthonormal computational basis states  $\{|x\rangle\}_{x=0}^{N-1}$  to a new set of orthonormal states, which we refer to as the *Fourier basis*  $\{|\bar{x}\rangle\}_{x=0}^{N-1}$ . This operation is defined as:

$$\text{QFT}|x\rangle = |\bar{x}\rangle = \frac{1}{\sqrt{N}} \sum_{y=0}^{N-1} e^{2\pi i \frac{xy}{N}} |y\rangle. \quad (1)$$

Each state  $|\bar{x}\rangle$  in the Fourier basis is an equal superposition of all computational basis states, distinguished only by their relative phases. Consequently, the Inverse Quantum Fourier Transform (iQFT) serves as the decoding operation that maps a state from the Fourier basis back to the computational basis:

$$\text{QFT}^{-1}|\bar{x}\rangle = |x\rangle. \quad (2)$$

Mathematically, the iQFT is the adjoint of the QFT operator ( $\text{QFT}^\dagger$ ). Its action on an arbitrary computational basis state  $|y\rangle$  is given by introducing a negative sign in the complex exponential:

$$\text{QFT}^{-1}|y\rangle = \frac{1}{\sqrt{N}} \sum_{x=0}^{N-1} e^{-2\pi i \frac{xy}{N}} |x\rangle. \quad (3)$$

This transformation is fundamental in quantum algorithms such as Quantum Phase Estimation (QPE) and Shor's algorithm, where the solution is encoded in the relative phases of the qubits (Fourier basis) and must be transformed back to the computational basis to be measured with high probability.

#### 2.1.1. Circuit Implementation

The decomposition of the iQFT into a quantum circuit consists of a structured sequence of Hadamard ( $H$ ) gates and two-qubit Controlled-Phase ( $CP$ ) rotations, followed by a SWAP network to reverse the order of the qubits. The specific circuit implementation considered in this work is illustrated in Figure 1.

The rotation angle applied to a target qubit  $i^\square$ , controlled by qubit  $i^\bullet$ , is determined by the logical index difference  $k$  between them, denoted as:

$$\theta(i^\bullet, i^\square) = \theta_{i^\square - i^\bullet} = -\frac{\pi}{2^{i^\square - i^\bullet}}. \quad (4)$$

$CP(\theta_k)$ , applies a diagonal phase shift depending on the index difference between the qubits ( $k = i^\square - i^\bullet$ ). For the inverse transform, the rotation angle is negative:

$$CP(\theta_k) = \text{diag}\left(1, 1, 1, e^{-i\frac{\pi}{2^k}}\right), \quad (5)$$

where  $k$  represents index difference between the control and target qubits in the register. The exact implementation requires  $O(n^2)$  such gates. However, as  $k$  increases, the rotation angle approaches zero.

$$\lim_{k \rightarrow \infty} \theta_k = 0. \quad (6)$$

This property is crucial for distributed implementations, as it allows for the truncation of small-angle rotations (approximate iQFT) to reduce inter-node communication, a concept we detail in subsequent sections.

To illustrate the specific connectivity pattern by these operations, Figure 2 describes the interactions between an arbitrary pair qubits,  $i^\bullet$  as control and qubit  $i^\square$  as target. The angle  $\theta$  applied follows the Eq. 4:

#### 2.1.2. Gate Complexity and Scaling

The computational cost of the exact iQFT is dominated by the number of two-qubit controlled-phase ( $CP$ ) rotations required to encode the relative phases. For an  $n$ -qubit register, the standard decomposition involves a sequence of operations where the  $j$ -th qubit (for  $j = 1, \dots, n$ ) acts as a control for  $n - j$  target qubits.

The total number of controlled-phase gates, denoted as  $N_{CP}$ , is determined by the summation of these interactions across the entire circuit:

$$N_{CP}(n) = \sum_{j=1}^{n-1} j = \frac{n(n-1)}{2}. \quad (7)$$

Consequently, the gate complexity scales quadratically with the system size, i.e.,  $N_{CP} \in \Theta(n^2)$ . While the number of Hadamard gates scales linearly as  $\Theta(n)$  and the final SWAP network requires  $\Theta(n)$  operations, the quadratic growth of the entangling  $CP$  gates presents the primary bottleneck for scalability.

Beyond gate count, the iQFT imposes demanding connectivity constraints on the underlying hardware topology. The algorithm dictates that every qubit  $i^\bullet$  must interact directly via a two-qubit gate with every other qubit  $i^\square$  (where  $i^\square > i^\bullet$ ) to apply the necessary phase shifts.

From a graph-theoretic perspective, the interaction graph of the iQFT corresponds to a complete graph  $K_n$ , where an edge exists between every pair of vertices.

This disparity between the algorithmic requirement (all-to-all) and physical constraints significantly increases the effective circuit depth and the total operation count in realistic implementations.

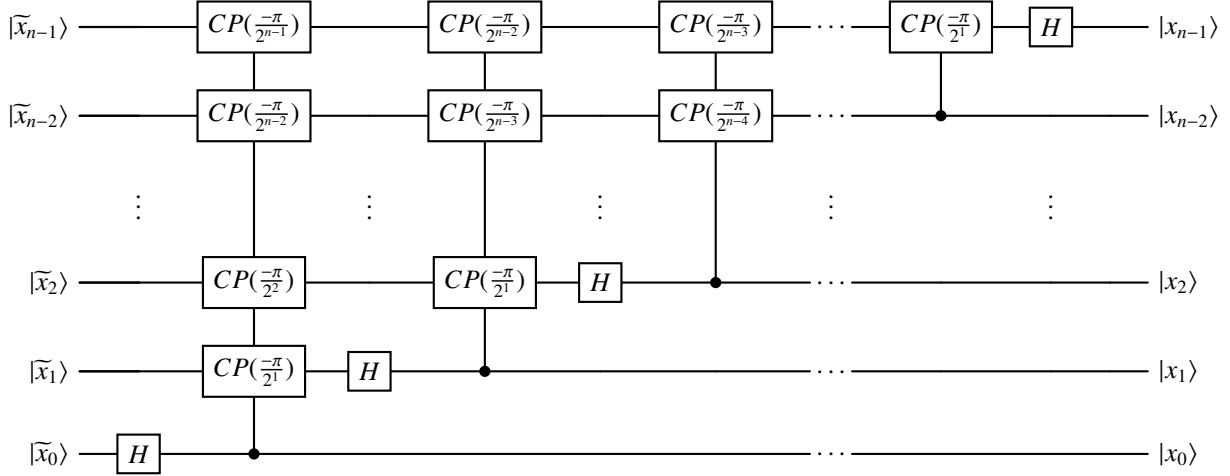


Figure 1: Circuit realization of the  $n$ -qubit Inverse Quantum Fourier Transform (iQFT). The circuit maps the input state from the Fourier basis  $|\tilde{x}\rangle$  to the computational basis  $|x\rangle$  using a sequence of Hadamard gates ( $H$ ) and controlled phases  $CP(\theta_k)$  where  $\theta_k = \pi/2^k$ .

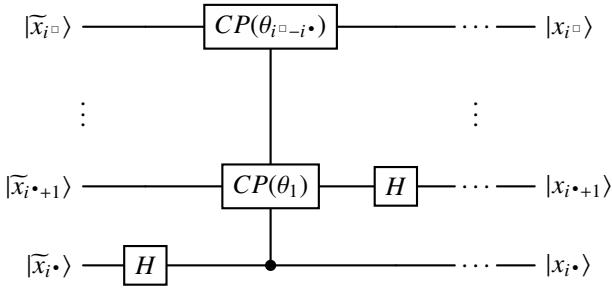


Figure 2: Interaction between the  $i^*$ -th qubit as control and the  $i^\square$ -th qubit as target within the iQFT sequence. The diagram highlights the Hadamard gate applied to  $|\tilde{x}_{i^\square}\rangle$  and the conditional phase rotation controlled by  $|\tilde{x}_{i^\square}\rangle$  acting on  $|\tilde{x}_{i^*}\rangle$ .

## 2.2. Distributed Quantum Computing: teledata and telegate

Scaling quantum computation beyond the qubit limits of a single processor requires the interconnection of multiple Quantum Processing Units (QPUs) into a distributed network. In such an architecture, the execution of a monolithic quantum circuit is partitioned across distinct nodes. To realize non-local interactions between qubits residing on physically separated QPUs, the system must rely on quantum communication channels and the distribution of entanglement [17, 18, 19].

We assume the network links are capable of generating and sharing Einstein-Podolsky-Rosen (EPR) pairs, specifically the Bell state  $|\Phi^+\rangle = \frac{1}{\sqrt{2}}(|00\rangle + |11\rangle)$ , between nodes. Utilizing this shared resource, two primary communication primitives are established to support distributed logic: *Teledata* [20] and *Telegate* [21, 22].

### 2.2.1. Teledata: state teleportation

The Teledata strategy, based on the standard quantum teleportation protocol, physically relocates the quantum state of a qubit from a source node  $A$  to a destination node  $B$ . This approach is necessary when the no-cloning theorem prevents the

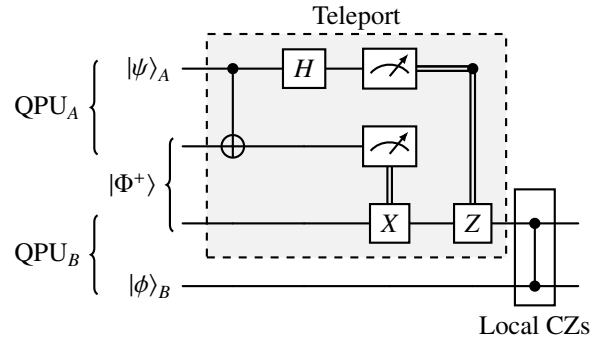


Figure 3: Circuit schematic of the *Teledata* protocol. The quantum state  $|\psi\rangle_A$  is teleported from QPU<sub>A</sub> to QPU<sub>B</sub> utilizing a shared EPR pair. Upon receiving the classical measurement outcomes for Pauli corrections ( $X, Z$ ), the state is reconstructed at the destination. This allows the subsequent interaction with  $|\phi\rangle_B$  (depicted here as a CZ gate) to be executed as a local operation, avoiding non-local gate overhead.

copying of quantum information, requiring the destruction of the state at the source to reconstruct it at the destination.

Mathematically, let  $|\psi\rangle_A = \alpha|0\rangle_A + \beta|1\rangle_A$  be the state to be transmitted. The system begins with the state  $|\psi\rangle_A$  and a shared EPR pair  $|\Phi^+\rangle_{AB}$  distributed across the nodes:

$$|\Psi_{total}\rangle = |\psi\rangle_A \otimes \frac{1}{\sqrt{2}}(|0\rangle_A|0\rangle_B + |1\rangle_A|1\rangle_B). \quad (8)$$

Node  $A$  performs a Bell-basis measurement on the qubit to be sent and its half of the entangled pair. This measurement collapses the global state and yields two classical bits,  $M_1, M_2 \in \{0, 1\}$ . These bits are transmitted via a classical channel to node  $B$ . To recover the original state  $|\psi\rangle$ , node  $B$  applies a Pauli correction operation  $X^{M_2}Z^{M_1}$  based on the received bits:

$$|\psi\rangle_B = X^{M_2}Z^{M_1}|\phi\rangle_B, \quad (9)$$

where  $|\phi\rangle_B$  is the post-measurement state at node  $B$ . The circuit implementation for this protocol is depicted in Figure 3.

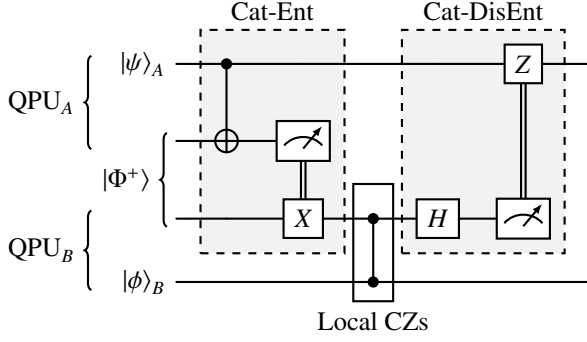


Figure 4: Circuit implementation of the *Telegate* protocol. This primitive executes a non-local controlled-Z gate between a control qubit  $|\psi_A\rangle$  in QPU<sub>A</sub> and a target  $|\phi_B\rangle$  in QPU<sub>B</sub> using a single shared EPR pair. The process involves an entanglement stage (Cat-Ent) to link the control to the channel, followed by the local interaction, and a disentanglement stage (Cat-DisEnt). Note the bidirectional classical communication required for the  $X$  and  $Z$  Pauli corrections.

- **Advantages:** The primary advantage of Teledata is that once the state  $|\psi\rangle$  is reconstructed at node  $B$ , it becomes local to that node. Consequently, an arbitrary number of subsequent local gates can be executed on  $|\psi\rangle$  without further inter-node communication penalties.
- **Disadvantages:** The protocol consumes one EPR pair and requires one round of classical communication. However, if the circuit logic requires the qubit to act as a control for a target back in node  $A$  (or another node) after its migration, the state must be teleported back. This “round-trip” operation doubles the cost, consuming a total of 2 EPR pairs and inducing additional latency.

### 2.2.2. Telegate: remote gate application

The *Telegate* protocol allows the execution of a non-local controlled unitary  $U$  between a control qubit  $q_A$  in node  $A$  and a target qubit  $q_B$  in node  $B$ . Unlike *Teledata*, this method does not transport the quantum information of the control qubit. Instead, it temporarily extends the superposition of the control across the network to mediate the interaction.

Let the initial state of the control qubit on QPU  $A$  be:

$$q_A : |\psi\rangle_A = \alpha|0\rangle_A + \beta|1\rangle_A, \quad \text{with } \alpha, \beta \in \mathbb{C}, \quad (10)$$

and the network shares an EPR pair

$$e_A, e_B : |\Phi^+\rangle_{AB} = \frac{1}{\sqrt{2}}(|0\rangle_A |0\rangle_B + |1\rangle_A |1\rangle_B) \quad (11)$$

The protocol proceeds in three distinct phases:

#### 2.2.2.1 Cat-Entanglement (Cat-Ent)

The goal of this phase is to share the amplitudes of the control qubit into the communication channel. First, a local CNOT is applied between the control  $q_A$  and the local EPR half  $e_A$ , followed by a  $Z$ -basis measurement on  $e_A$  (outcome  $m_A$ ) and a classical feed-forward correction  $X^{m_A}$  on  $e_B$ .

Mathematically, starting from the joint state:

$$|\Psi_0\rangle = (\alpha|0\rangle_A + \beta|1\rangle_A) \otimes |\Phi^+\rangle_{AB}. \quad (12)$$

1. Apply  $\text{CNOT}_{A \rightarrow e_A}$ :

$$|\Psi_1\rangle \propto \alpha|0\rangle_A(|00\rangle_{AB} + |11\rangle_{AB}) + \beta|1\rangle_A(|10\rangle_{AB} + |01\rangle_{AB}).$$

Note that the parity of the EPR pair is now correlated with the amplitude  $\beta$ .

2. Measure  $e_A$  and correct  $e_B$ .

- If  $m_A = 0$ , the state collapses to terms with  $|0\rangle_A$ .
- If  $m_A = 1$ , it collapses to terms with  $|1\rangle_A$  and the  $X$  correction flips  $e_B$ .

In both cases, the system converges to the *cat-entangled* state:

$$|\Psi_{Cat}\rangle = \alpha|0\rangle_A|0\rangle_{e_B} + \beta|1\rangle_A|1\rangle_{e_B}. \quad (13)$$

**Interpretation:** The probability amplitudes  $\alpha$  and  $\beta$  are now *shared* between the original control  $q_A$  and the remote EPR proxy  $e_B$ . This strictly correlated state  $|k\rangle_A|k\rangle_{e_B}$  implies that  $e_B$  can be used as control of  $q_A$  in the computational basis.

#### 2.2.2.2 Local Interaction

With the amplitudes shared, node  $B$  can perform the intended controlled operation using  $e_B$  as the control. Let  $|\phi\rangle_B$  be the state of the target qubit. The operator  $CU$  is applied locally between  $e_B$  and  $|\phi\rangle_B$ :

$$CU_{e_B, q_B} = |0\rangle_{e_B}\langle 0| \otimes \mathbb{I}_{q_B} + |1\rangle_{e_B}\langle 1| \otimes U_{q_B} \quad (14)$$

$$\begin{aligned} |\Psi_{int}\rangle &= CU_{e_B, q_B} [(\alpha|0\rangle_A|0\rangle_{e_B} + \beta|1\rangle_A|1\rangle_{e_B}) \otimes |\phi\rangle_B] \\ &= \alpha|0\rangle_A|0\rangle_{e_B}(\mathbb{I}|\phi\rangle_B) + \beta|1\rangle_A|1\rangle_{e_B}(U|\phi\rangle_B). \end{aligned} \quad (15)$$

Since  $e_B$  is perfectly correlated with  $A$  (i.e.,  $e_B$  is 1 if and only if  $A$  is 1), triggering the gate with the proxy  $e_B$  is mathematically equivalent to triggering it with the original qubit  $A$ . The logical state of the target has evolved correctly according to the superposition of  $A$ .

#### 2.2.2.3 Cat-Disentanglement (Cat-DisEnt)

Finally, the protocol must decouple the channel to restore the control qubit. A Hadamard gate is applied to  $e_B$ , transforming the basis:  $|0\rangle \rightarrow |+\rangle, |1\rangle \rightarrow |-\rangle$ .

$$|\Psi'\rangle = \alpha|0\rangle_A |+\rangle_{e_B} |\phi\rangle_B + \beta|1\rangle_A |-\rangle_{e_B} (U|\phi\rangle_B) \quad (16)$$

Regrouping terms by the state of  $e_B$ :

$$\begin{aligned} |\Psi'\rangle &\propto |0\rangle_{e_B} (\alpha|0\rangle|\phi\rangle + \beta|1\rangle U|\phi\rangle) \\ &\quad |1\rangle_{e_B} (\alpha|0\rangle|\phi\rangle - \beta|1\rangle U|\phi\rangle) \end{aligned} \quad (17)$$

A measurement of  $e_B$  yields  $m_B$ . If  $m_B = 1$ , a phase flip (minus sign) has occurred on the  $\beta$  term. This is corrected by sending  $m_B$  to node  $A$  and applying  $Z^{m_B}$  on  $q_A$ . The final state is:

$$|\Psi_{final}\rangle = (\alpha|0\rangle_A + \beta|1\rangle_A) \otimes \text{controlled-}U(|\phi\rangle_B) \quad (18)$$

Thus, the non-local gate is realized with a single EPR pair, at the cost of two classical communication rounds ( $m_A$  and  $m_B$ ).

- **Advantages:** Telegate is resource-efficient for isolated non-local interactions, as it executes a controlled operation consuming only a single EPR pair (1 EPR). This is half the entanglement cost required to teleport a qubit, perform the gate locally, and teleport it back (Teledata round-trip).
- **Disadvantages:** The protocol incurs higher synchronization overhead. It requires a bidirectional exchange of classical information to coordinate the sequence: a synchronization signal to initiate the remote sequence and the transmission of measurement results to finalize the gate with Pauli corrections. This exposes the circuit execution to the latency of two distinct classical communication events, potentially stalling the pipeline if not managed efficiently.

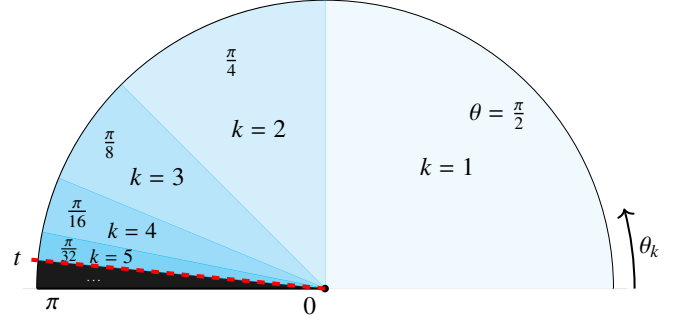


Figure 5: Geometric representation of the accumulated phase in the iQFT showing the rapid decay of rotation angles  $\theta_k = \pi/2^k$ . The explicit sectors for  $k = 1$  to  $k = 5$  are shown as example. The threshold cutoff  $t$  (red dashed line) indicates the truncation point; interactions beyond this limit (black sector) contribute a negligible phase shift bounded by  $\varepsilon\pi$ .

### 2.3. Approximate QFT<sup>-1</sup> with phase fraction $\varepsilon$

The exact formulation of the QFT<sup>-1</sup> entails a complete interaction graph, requiring a two-qubit controlled-phase rotation  $CP(\theta_k)$  for every pair of qubits, where  $k$  denotes the index difference between the control and target qubits ( $i^\square - i^\star$ ). As detailed in Section 2.1, the rotation angle is given by:

$$\theta_k = -\frac{\pi}{2^k}. \quad (19)$$

A critical observation for optimization is the exponential decay of these rotation angles as  $k$  increases. The magnitude of the phase shift is reduced by half for each increment. Consequently, the total phase accumulated by the last target qubit  $n - 1$ , assuming all possible control qubits are in the state  $|1\rangle$ , follows a geometric progression:

$$\varphi(n - 1) = \sum_{k=1}^{n-1} \theta_k = \sum_{k=1}^{n-1} \frac{\pi}{2^k} = \pi \left(1 - \frac{1}{2^{n-1}}\right). \quad (20)$$

As  $n \rightarrow \infty$ , this sum converges to  $\pi$ , representing a maximum phase shift of  $180^\circ$ . However, the contributions from distant qubits (large  $k$ ) become vanishingly small. This behavior is illustrated in Figure 5, which visualizes how the significance of the rotation diminishes rapidly with  $k$ .

To reduce the gate count, we can employ an approximate QFT<sup>-1</sup> by truncating these negligible rotations. To bound the algorithmic error introduced by this truncation, we define a fractional phase tolerance  $\varepsilon$ , guaranteeing that the total accumulated phase of the discarded gates strictly does not exceed  $\varepsilon\pi$ . Based on this tolerance, we introduce a threshold parameter  $t$ , such that all  $CP(\theta_k)$  gates with  $k > t$  are discarded. The unitary operator for the approximate transform, denoted as  $\tilde{U}$ , differs from the exact operator  $U$  by the omission of these small-angle gates.

To assess the impact of gate truncation, we partition the summation from Eq. 20 into two distinct components based on the selected threshold  $t$ . The first component, evaluated as  $\varphi(t)$ , represents the implemented rotation, while the second component encapsulates the discarded terms. This decomposition allows us to express the exact phase as:

$$\varphi(n - 1) = \varphi(t) + \sum_{k=t+1}^{n-1} \theta_k. \quad (21)$$

Consequently, the deviation between the exact and the implemented rotation is determined entirely by the sum of the truncated angles. By substituting the specific rotation values  $\theta_k = \pi/2^k$ , we obtain:

$$\varphi(n - 1) - \varphi(t) = \sum_{k=t+1}^{n-1} \frac{\pi}{2^k}. \quad (22)$$

Using the next property of the geometric series:

$$\sum_{k=t+1}^n 2^{-k} = 2^{-t} - 2^{-n}, \quad (23)$$

applying this property to the truncated sum yields the final analytical expression for the approximation error:

$$\varphi(n - 1) - \varphi(t) = \pi \left( \frac{1}{2^t} - \frac{1}{2^{n-1}} \right). \quad (24)$$

In addition, an upper bound can be defined by ignoring  $1/2^{n-1}$  when  $n \rightarrow \infty$ . This is useful for simplifying subsequent calculations to bound  $t$ :

$$\varphi(n - 1) - \varphi(t) = \frac{\pi}{2^t}. \quad (25)$$

To ensure that the approximation does not exceed the specified tolerance  $\varepsilon\pi$ , we require  $\varphi(n - 1) - \varphi(t) \leq \varepsilon\pi$ . Solving for the threshold  $t$ , we obtain the cutoff condition:

$$2^t \geq \frac{\pi}{\varepsilon\pi} \implies t \geq \log_2 \left( \frac{1}{\varepsilon} \right) = -\log_2(\varepsilon). \quad (26)$$

Thus, to maintain an accuracy of  $\varepsilon$ , it is sufficient to retain only those controlled-phase gates where

$$k \geq t = \lceil -\log_2(\varepsilon) \rceil. \quad (27)$$

This transforms the gate complexity from  $O(n^2)$  to  $O(n \cdot t)$ , offering a significant reduction for large  $n$  while preserving algorithmic fidelity.

### 3. Methods and methodology

#### 3.1. Distributed iQFT across $N$ nodes

To distribute the iQFT across a networked architecture, we must restructure the monolithic circuit into a sequence of operations that distinguishes between intra-node (local) and inter-node (distributed) dependencies.

To formalize the distributed architecture, we define a quantum circuit characterized by the following parameters:

- **Network dimension:** The system consists of  $P$  nodes, indexed by the identifier  $p \in \{0, 1, \dots, P-1\}$ . To explicitly distinguish functional roles during distributed quantum operations, we introduce the modifiers  $p^\bullet$  to denote a node acting as a control and  $p^\square$  to denote a target node.
- **Node capacity:** We assume a homogeneous distribution where each node hosts exactly  $Q$  local qubits. Consequently, the total logical register size is  $n = P \cdot Q$ .
- **Qubit state notation:** We introduce the notation  $|\tilde{x}_q^{(p)}\rangle$  to denote the state of the  $q$ -th qubit residing in the  $p$ -th node. Here,  $q \in \{0, 1, \dots, Q-1\}$  represents the local index of the qubit within its host node. Similar to the node notation, we use  $q^\bullet$  and  $q^\square$  to designate a control and target qubit, respectively. To simplify complex mathematical expressions and improve readability, we define the shorthand notation  $|\tilde{x}_q^{(p^\bullet)}\rangle$  as strictly equivalent to  $|\tilde{x}_q^{(p^\bullet)}\rangle$ , concisely indicating that both the specific qubit and its host node serve the control role. The same equivalence applies to the target notation  $|\tilde{x}_q^{(p^\square)}\rangle \equiv |\tilde{x}_q^{(p^\square)}\rangle$ .
- **Global mapping:** The global index of any given qubit within the complete  $n$ -qubit register can be recovered through the linear mapping function  $I(q, p) = p \cdot Q + q$ .

The standard iQFT decomposition (as seen in Section 2.1) requires applying Controlled-Phase (CP) rotations between every pair of qubits. In a distributed setting, these interactions fall into two distinct categories:

1. **Local blocks:** Interactions where both the control and target qubits reside within the same node  $p$  (so,  $p^\square = p^\bullet$ ). These operations can be executed entirely within the QPU without utilizing the quantum network.
2. **Communication blocks:** Interactions where the control qubit resides in node  $p^\bullet$  and the target qubit resides in node  $p^\square$  (with  $p^\square \neq p^\bullet$ ). These require entanglement-assisted communication primitives to realize the non-local phase shifts.

Figure 6 illustrates this segmented architecture for a specific case of  $P = 3$  nodes with  $Q = 2$  qubits each ( $n = 6$ ). The structure reveals a distinct execution pattern: each node  $p$  must first apply a series of *Communication blocks*, interacting sequentially with nodes  $p^\bullet < p$ . Only after these non-local phases are applied can the node proceed to execute its *Local block*. Crucially, this local component can be identified as a

lower-order iQFT instance; specifically, it corresponds to a local iQFT acting on the  $Q$  qubits assigned to the node, executed without external dependencies.

The generalized interaction logic is depicted in Figure 7. For a control qubit  $|\tilde{x}_i^{(p)}\rangle^\bullet$  in node  $p^\bullet$  and a target qubit  $|\tilde{x}_i^{(p)}\rangle^\square$  in a remote node  $p^\square$ , the rotation angle depends on the global index difference between them. Assuming the node index  $p^\square$  represents the higher-order significance bits, the index difference  $k$  between the control qubit  $q^\bullet$  of node  $p^\bullet$  and the target qubit  $q^\square$  of node  $p^\square$  is derived from their global indices:

$$I^\bullet = p^\bullet \cdot Q + q^\bullet, \quad I^\square = p^\square \cdot Q + j^\square. \quad (28)$$

The rotation index  $k$  corresponds to the difference  $|I^\square - I^\bullet|$ . In the standard decomposition where controls are applied from distant nodes  $p < p'$ , the specific rotation angle applying Eq. 4 is given by:

$$\theta(I^\bullet, I^\square) = \frac{-\pi}{2^{Q(p^\square - p^\bullet) + (q^\square - q^\bullet)}}. \quad (29)$$

This formulation allows us to map the abstract algorithm directly to physical link requirements. The communication blocks effectively group these interactions.

To formally demonstrate that the intra-node operations constitute a standard iQFT of dimension  $Q$  (local block), we apply the locality condition  $p^\bullet = p^\square$  to the generalized rotation formula derived in Eq. 29. When both control and target qubits reside in the same node, the term  $Q(p^\square - p^\bullet) = 0$ . Consequently, the rotation angle  $\theta$  simplifies to depend solely on the local indices  $q^\bullet$  and  $q^\square$ :

$$\theta_{p^\square = p^\bullet} = \frac{-\pi}{2^{Q(0) + (q^\square - q^\bullet)}} = \frac{-\pi}{2^{q^\square - q^\bullet}}, \quad \text{for } q^\square > q^\bullet. \quad (30)$$

This expression is mathematically identical to the phase shift definition of the monolithic iQFT shown in Figure 7 and Eq. 4, specifically for a difference  $k = i^\square - i^\bullet$ . Since the indices  $i$  range from 0 to  $Q-1$ , the set of operations within this block generates exactly the interaction graph of a  $Q$ -qubit iQFT. Thus, the *Local Block* is equivalent to an iQFT( $Q$ ), verifying that no inter-node communication is required for these specific gates.

Figure 8 depicts the generalized execution schedule for an arbitrary node  $p$  within the network. The quantum circuit is abstracted into a sequence of communicative layers followed by a local computation (as shown in Figure 6).

Instead of treating non-local interactions as isolated gates, the interaction with preceding nodes is structured into communicative blocks denoted by  $\mathbf{CP}(\Theta_d)$ . Here,  $d$  represents the logical distance to the control node (i.e., interacting with node  $p^\square = p^\bullet + d$ ). Each block encapsulates the complete set of remote controlled-phase rotations required between the  $Q$  qubits of the target node  $p^\square$  and the  $Q$  qubits of the control node  $p^\square - d = p^\bullet$ .

Mathematically,  $\Theta_d$  is defined as the set of all phase rotations to be applied within that specific block. Following the generalized rotation derived in Eq. 29, this set is strictly formulated as:

$$\Theta_d = \{\theta(I(q^\bullet, p^\bullet), I(q^\square, p^\square)) \mid p^\square = p^\bullet + d\}, \quad (31)$$

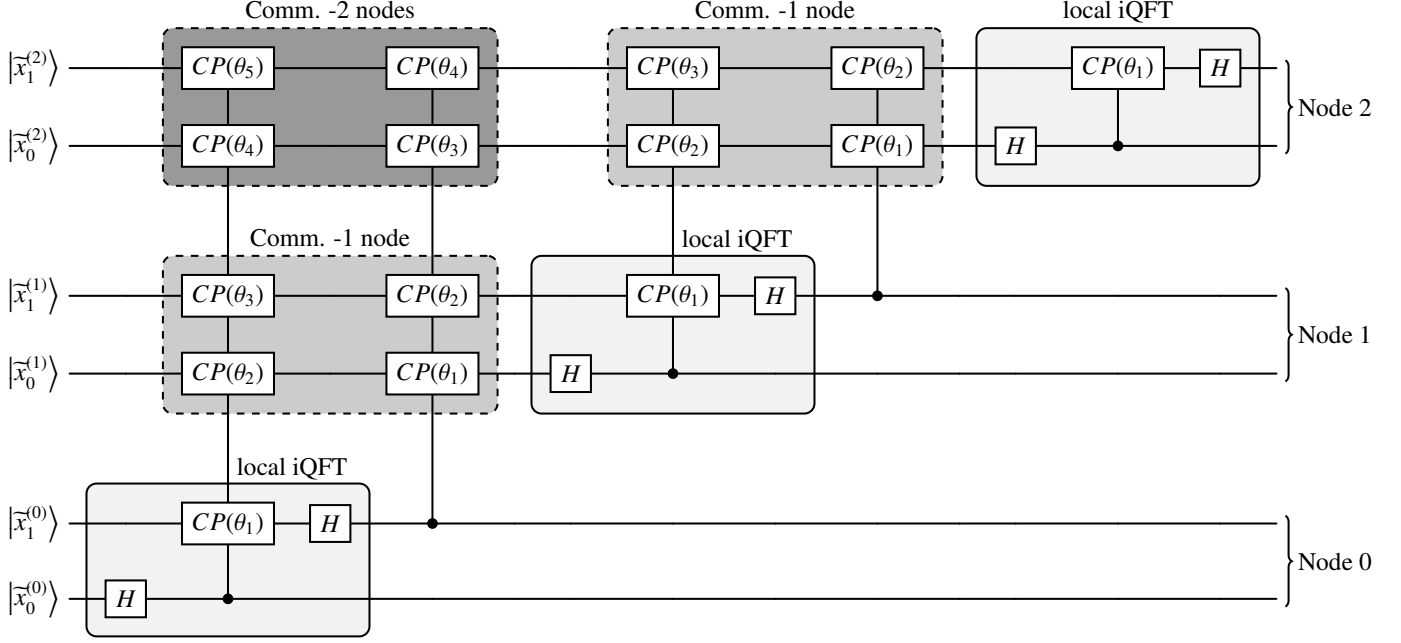


Figure 6: Distributed decomposition of a 6-qubit iQFT across 3 nodes ( $p = 0, 1, 2$ ). The circuit is restructured into Local iQFT blocks (light gray), which require no external communication, and Communication Blocks (darker gray), where Node  $p$  interacts with qubits from previous nodes  $p' < p$ . The phase angles follow  $\theta_k = \pi/2^k$ .

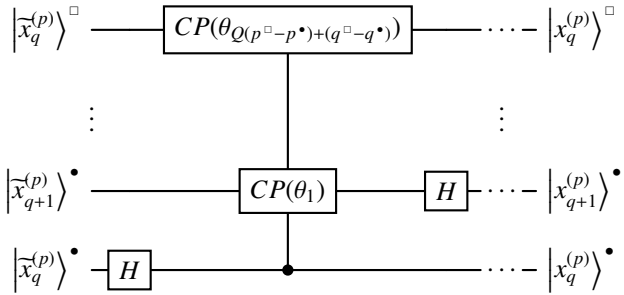


Figure 7: Generic interaction between a target qubit  $q^\square$  in node  $p^\square$  and a control qubit  $q^\bullet$  in a distant node  $p^\bullet$ . The rotation angle is determined by the global index difference, formalized as  $\theta_k$  where  $k = \frac{\pi}{2^k}$ .

where  $q^\square$  denotes the qubit index in the target register (node  $p^\square$ ) and  $q^\bullet$  the index in the control register (node  $p^\bullet - d = p^\bullet$ ). This formulation ensures that all cross-node dependencies are satisfied for the given distance.

As shown in the circuit, the sequence proceeds from the most distant interactions ( $d = p$ , corresponding to node 0) to the nearest neighbor ( $d = 1$ , corresponding to node  $p - 1$ ).

### 3.2. Communication Efficiency: block pruning strategy

While the standard approximate iQFT reduces the total gate count by discarding small-angle rotations, its impact is particularly transformative in a distributed setting. In monolithic architectures, removing a gate merely saves execution time. However, in a distributed architecture, the primary bottlenecks are the generation of entanglement (EPR pairs) and the latency of classical communication rounds. Therefore, the optimization

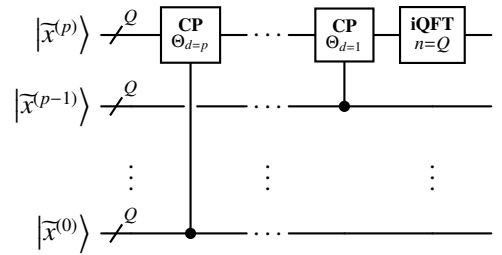


Figure 8: Generic interaction between nodes, execution model for an arbitrary node  $p$ . The circuit illustrates the sequential application of communication blocks  $\mathbf{CP}$ , starting from the most distant dependency (Node 0,  $d = p$ ) up to the nearest (Node  $p - 1$ ,  $d = 1$ ). The execution of this sequence assumes that all previous nodes  $0, \dots, p - 1$  have already initiated their corresponding operations to act as controls. The process concludes with a local inverse QFT on the  $Q$  qubits of node  $p$ .

goal shifts from simply reducing  $N_{CP}$  to minimizing the number of active inter-node links.

We leverage the geometric decay of the rotation angles derived in Section II-C to define a *communication horizon*. Recall that for a target accuracy  $\varepsilon$ , any controlled-phase rotation  $CP(\theta_k)$  with distance  $k > t$  can be approximated as the identity, where  $t = \lceil -\log_2(\varepsilon) \rceil$  (Eq. 27). We apply this threshold to the coarse-grained communication blocks  $\mathbf{CP}(\Theta_d)$  (Eq. 31) defined in Section III-A.

A communication block  $\mathbf{CP}(\Theta_d)$  encapsulates interactions between a target node  $p^\square$  and a control node at distance  $d$ . The set of rotation indices involved in this block is defined in the Eq. 31. To determine the relevance of the entire block, we consider the *maximum interaction strength* within it, which corresponds to the smallest qubit distance  $k_{min}$  (i.e., the largest rota-

tion angle). This occurs between the least significant qubit of the target node ( $q^\square = 0$ ) and the most significant qubit of the control node ( $q^\bullet = Q - 1$ ), applying Eq. 29:

$$k_{\min}(d) = Q \cdot (p^\square - p^\bullet) + (0) - (Q - 1) = Q(d - 1) + 1. \quad (32)$$

If this strongest interaction falls below the significance threshold (i.e., if  $k_{\min}(d) > t$ ), then every other interaction in the block will also satisfy  $k > t$ . Consequently, the entire communication block becomes negligible and can be pruned from the schedule.

We formalized this by deriving a maximum communication distance, denoted as  $d_{\max}$ , which bounds the number of remote nodes any given node must communicate with. Setting the condition  $k_{\min}(d_{\max}) \leq t$ , we solve for  $d$ :

$$Q(d_{\max} - 1) + 1 \leq t \implies d_{\max} \leq \frac{t - 1}{Q} + 1. \quad (33)$$

Substituting  $t$  from Eq. 27, we obtain the communication horizon as a function of the error tolerance  $\varepsilon$  and the node capacity  $Q$ :

$$d_{\max} = \left\lceil \frac{\lceil -\log_2(\varepsilon) \rceil - 1}{Q} \right\rceil + 1. \quad (34)$$

This derivation implies that a node  $p$  only requires entanglement links with its  $d_{\max}$  nearest neighbors. Any potential communication block with distance  $d > d_{\max}$  is strictly pruned.

This strategy has profound implications for scalability. While the exact distributed iQFT requires an all-to-all communication topology (where node  $p$  communicates with all  $0 \dots p - 1$ ), our optimized approach bounds the connectivity degree. The number of non-local blocks per node transitions from growing linearly with the network size ( $O(P)$ ) to being bounded by a constant ( $O(d_{\max})$ ), effectively localizing the communication overhead regardless of the total number of nodes in the system.

### 3.2.0.1 Interpretation

To illustrate the practical impact, consider a network composed of nodes with capacity  $Q = 4$  qubits. Targeting a high algorithmic fidelity with  $\varepsilon = 10^{-5}$ , the phase truncation threshold is  $t \approx 17$ . Applying Eq. 34, the communication horizon is bounded by  $d_{\max} = 5$ . This implies that in a large-scale network (e.g., 100 nodes), Node 99 is not required to establish costly long-range entanglement links with Nodes 0 through 93; it strictly needs to coordinate with its 5 nearest predecessors (Nodes 94–98). Interactions beyond this horizon contribute negligible phase shifts and are safely discarded, drastically reducing the demand on quantum repeater networks.

## 3.3. Metrics evaluated

To rigorously assess the impact of the proposed distributed architecture and optimization strategies, we quantify performance using the following set of metrics. These metrics are designed to evaluate the trade-offs between algorithmic fidelity, communication resources, and circuit locality.

### 3.3.1. Fidelity vs. Threshold

We evaluate the accuracy of the approximate distributed iQFT by computing the state fidelity, defined as:

$$\mathcal{F} = |\langle \psi_{\text{ideal}} | \psi_{\text{approx}} \rangle|^2, \quad (35)$$

where  $|\psi_{\text{ideal}}\rangle$  is the output state of the exact transform and  $|\psi_{\text{approx}}\rangle$  is the output of the pruned circuit. This metric is analyzed as a function of the pruning threshold  $t$ . The objective is to validate the theoretical error model derived in Section 2.3 by comparing the fidelity obtained from full state-vector simulations against the theoretical lower bound implied by the chosen accuracy parameter  $\varepsilon$ .

**What does it prove?** This serves to empirically validate the theoretical error bound and cutoff condition derived in Section 2.3 (Eq. 27).

### 3.3.2. Scalability of entanglement resources (EPR per Node)

This metric quantifies the aggregate cost of inter-node communication required to execute the algorithm. We measure the total count of EPR pairs consumed across the entire network during the circuit execution. We analyze the behavior of this cost as a function of the pruning threshold  $t$ , comparing the baseline distributed iQFT against the optimized implementation.

**What does it prove?** This metric directly demonstrates the global communication savings achieved by the pruning strategy described in Section 3.2.

### 3.3.3. Accuracy under connectivity constraints

Suppose hardware limitation of a fixed communication horizon  $d_{\max}$  (the maximum distance between interacting nodes) and a specific node capacity  $Q$ , we analyze the achievable algorithmic accuracy. By inverting the relationship established in the block pruning strategy, we determine the minimum error  $\varepsilon$  that can be guaranteed when the communication topology is restricted.

**What does it prove?** This analysis confirms the feasibility of the bounded interaction model and the communication horizon ( $d_{\max}$ ) proposed in Section 3.2.

### 3.3.4. Coupling Ratio

We define the Coupling Ratio  $\eta$  as the quotient between the number of remote controlled-phase gates (inter-node) and local controlled-phase gates (intra-node). This metric serves as a proxy for the degree of independence of the nodes. We analyze how  $\eta$  evolves with respect to the node capacity  $Q$ , the total network size  $P$ , and the approximation tolerance  $\varepsilon$ .

$$\eta(Q, P, \varepsilon) = \frac{N_{CP}^{\text{remote}}}{N_{CP}^{\text{local}}} \quad (36)$$

The objective is to try to achieve a  $\eta \rightarrow 0$  in the distributed algorithm.

**What does it prove?** This demonstrates the effectiveness of the distributed decomposition in Section 3.1 in clustering operations locally to minimize network latency.

### 3.3.5. Communication overhead

To quantify the operational penalty introduced by the network protocols, we define the *Communication Overhead* ( $\gamma$ ). This metric is calculated as the ratio between the number of physical operations dedicated exclusively to quantum communication ( $N_{\text{comm}}$ ) and the number of logical computational gates ( $N_{\text{comp}}$ ):

$$\gamma = \frac{N_{\text{comm}}}{N_{\text{comp}}} \quad (37)$$

In the context of the *Telegate* protocol utilized in this work,  $N_{\text{comm}}$  encompasses all auxiliary operations necessary for state transfer, including Bell pair generation, entanglement swapping operations (CNOTs), and measurement-dependent corrections. Conversely,  $N_{\text{comp}}$  refers strictly to the logical controlled-phase rotations required by the iQFT algorithm. A visual decomposition distinguishing between these communication-specific overheads and the fundamental computational gates is presented in Figure 4. It is important to emphasize that  $\gamma$  is a global metric, representing the aggregate overhead of the distributed execution rather than a per-node average.

**What does it prove?** This metric exposes the communication cost of the distributed implementation, quantifying the exact ratio of physical overhead operations required to execute a single useful logical gate.

### 3.4. Experimental methodology

To validate the proposed distributed architecture and the efficiency of the pruning strategy, we implemented the distributed iQFT algorithm utilizing the Qiskit software development kit. The numerical simulations were performed using the statevector simulator backend provided by Qiskit Aer. This simulator performs an ideal execution of the quantum circuit, computing the exact final quantum state vector  $|\psi_{\text{final}}\rangle$  rather than a probability distribution of measurement outcomes.

The choice of a state-vector simulation is essential for this study for two primary reasons: first, it allows for the precise calculation of the algorithmic fidelity  $\mathcal{F}$  by computing the overlap with the ideal mathematical output, enabling a direct verification of the theoretical error bounds and threshold equations derived in Section II-C. Second, it permits the exact tracking of entanglement resources without the statistical noise associated with shot-based sampling.

All experiments were conducted on the High-Performance Computing cluster of the *Centro Singular de Investigación en Tecnoloxías Intelixentes* (CiTIUS)<sup>1</sup>. Specifically, the simulations were executed on a dedicated compute node designed for memory-intensive workloads, equipped with the following specifications:

- **Processors:** 4 × Intel Xeon Gold 6248 CPUs @ 2.50GHz (20 cores per socket, totaling 80 physical cores).
- **Memory:** 1 TB of RAM.

This high-memory configuration is critical for the study, as the memory requirements for state-vector simulations scale exponentially with the number of qubits ( $16 \times 2^n$  bytes). The available 1 TB of RAM enabled the simulation of distributed systems with sufficient qubits to analyze the asymptotic behavior of the communication horizon  $d_{\text{max}}$  and the locality ratio  $\eta$ .

## 4. Results

### 4.1. Fidelity vs. Threshold validation

Figure 9 illustrates the infidelity, defined as  $1 - \mathcal{F}$  (Eq. 35), as a function of the pruning threshold  $t$  (Eq. 27) for system size of  $Q = 18$  qubits. The data is presented on a semilogarithmic scale to accommodate the wide dynamic range of the error, which spans from approximately  $10^{-1}$  to  $10^{-10}$ .

#### 4.1.1. Exponential Convergence

The linearity of the curves in the semilogarithmic plot indicates that the infidelity decays exponentially with a linear increase in the threshold  $t$ . This behavior confirms the efficacy of the proposed pruning strategy: a moderate increase in the threshold parameter yields a reduction in the final state error by several orders of magnitude. For instance, in the  $Q = 18$  case, increasing the threshold from  $t = 4$  to  $t = 10$  suppresses the error by nearly four orders of magnitude.

#### 4.1.2. Discrepancy between Simulation and Theory

A consistent divergence is observed between the numerical simulations and the analytical predictions. As depicted in Figure 9, the simulated infidelity (solid lines) remains strictly bounded by the theoretical error estimates (dashed lines) derived in Eq. 22.

This discrepancy is attributable to the conservative nature of the theoretical bound, which is derived under a *worst-case scenario* assumption. The theoretical upper bound assumes that every pruned controlled-phase gate,  $CP(\theta)$ , introduces its maximal possible error. Physically, this corresponds to the scenario where the control and target qubits are invariably in the state  $|1\rangle$ , maximizing the phase displacement.

However, during the actual execution of the Distributed iQFT, the system occupies a superposition of computational basis states. For any subspace of the wavefunction where the control qubit is in the state  $|0\rangle$ , the  $CP(\theta)$  gate acts as the identity operator ( $I$ ). Consequently, the removal of the gate in these subspaces introduces zero error.

### 4.2. Reduction of entanglement consumption

Figure 10 presents a comparative analysis of the entanglement resources required for the distributed iQFT, expressed as the number of EPR pairs generated *per node*. The results are depicted as heatmaps varying with the local system size ( $Q$ ) and the number of computing nodes ( $P$ ) for three distinct scenarios: the unbounded case (no pruning) and two pruned configurations with thresholds  $t = 7$  and  $t = 3$ .

<sup>1</sup>More information about the HPC cluster: <https://wiki.citius.gal/centro:servizos:hpc>

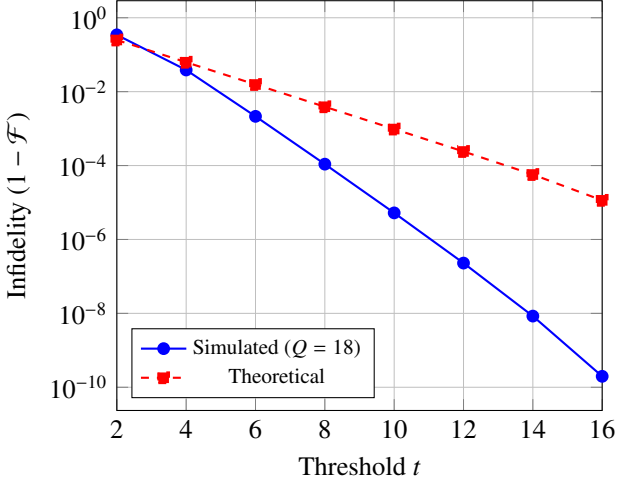


Figure 9: Analysis of the algorithmic infidelity ( $1 - \mathcal{F}$ ) as a function of the pruning threshold  $t$  for local register size  $Q = 18$ . The data is plotted on a semilogarithmic scale to visualize the **exponential decay** of the error. Solid lines represent the results obtained from full state-vector simulations, while dashed lines correspond to the theoretical error bounds derived in Eq. 27.

#### 4.2.1. Per-Node Resource Scaling

It is crucial to emphasize that the metric displayed corresponds to the EPR pairs generated *per individual node*. While the total entanglement consumption across the entire network would naturally scale with the number of nodes  $P$ , the per-node burden provides a more insightful measure of the local communication overhead and memory requirements. As observed in the leftmost panel (unbounded case), without pruning, the resource demand per node grows linearly with both  $Q$  and  $P$ , reflecting the dense connectivity of the standard iQFT circuit.

#### 4.2.2. Impact of Threshold Pruning

The central and rightmost panels of Figure 10 demonstrate the efficacy of the proposed pruning strategy. By applying a filtering threshold  $t$ , the initially quadratic growth of the total EPR count (reflected here as a linear increase per node) is effectively suppressed.

Consistent with the theoretical analysis in Section 3.2, the introduction of the threshold acts as a cutoff for long-distance or low-amplitude interactions. For stricter thresholds (e.g.,  $t = 3$ ), the number of EPR pairs per node saturates rapidly, becoming independent of the system size  $P$  for large networks. This drastic reduction confirms that the communication complexity can be bounded, transforming the global all-to-all entanglement requirement into a localized resource consumption pattern, thereby making the implementation scalable for large distributed quantum architectures.

### 4.3. Coupling ratio

To assess the computational efficiency of the distributed implementation relative to the communication overhead, we analyze the *Coupling ratio* ( $\eta$  defined in Eq. 36).

#### 4.3.1. High locality

In distributed quantum architectures, the quantum interconnect bandwidth and latency constitute the primary performance bottlenecks, often orders of magnitude slower than local gate operations. Consequently, maximizing data locality is paramount. An ideal distributed algorithm should strive for  $\eta \rightarrow 0$ , indicating that the computational workload is dominated by local processing rather than inter-node data transfer. Minimizing this ratio is essential to prevent the communication network from becoming the limiting factor in the total execution time.

#### 4.3.2. Impact of pruning on locality

Figure 11 illustrates the evolution of  $\eta$  as a function of the pruning threshold  $t$ . In the standard, unpruned iQFT, the ratio remains constant or grows with system size due to the dense connectivity of the algorithm. However, the application of the threshold  $t$  significantly improves this metric.

A central contribution of this work is the establishment of the communication horizon,  $d_{\max}(Q, \epsilon)$  (Eq. 34), which acts as a decisive control parameter for the network overhead the system is willing to tolerate.

Since the amplitude of the controlled-phase rotation  $\theta_k = \pi/2^k$  decays exponentially with the logical distance  $k$ , the pruning threshold  $t$  effectively imposes a hard limit on the interaction range. This mechanism preferentially filters out long-range remote operations—which typically correspond to high  $k$  and thus negligible phase shifts. Consequently,  $d_{\max}$  serves as a tuning parameter that drastically reduces the numerator  $N_{CP}^{\text{remote}}$  by enforcing this horizon, while preserving the majority of significant local interactions ( $N_{CP}^{\text{local}}$ ).

### 4.4. Accuracy under connectivity constraints

Figure 12 depicts the impact of imposing a fixed communication horizon  $d_{\max}$  on the algorithmic accuracy. The heatmaps quantify the theoretical error bound defined in Eq. 22 as a function of the local node capacity ( $Q$ ) and the maximum allowed communication distance ( $d_{\max}$  defined in Eq. 34). This analysis provides a crucial design guide for determining the minimal connectivity required to achieve a target precision.

#### 4.4.1. Rapid error convergence

The results demonstrate that the approximation error decays precipitously as the communication horizon increases. Even for moderate horizon values, the fidelity of the distributed iQFT remains high. For instance, in a system with local capacity  $Q = 9$  qubits per node, restricting the interaction range to just  $d_{\max} = 2$  neighboring nodes yields an error bound of approximately  $2^{-10}$ . This indicates that extending the connectivity beyond a small neighborhood (e.g.,  $d_{\max} \approx 3$  or 4) provides diminishing returns in accuracy while incurring significant communication costs. Consequently, a highly localized topology is sufficient for most practical applications.

#### 4.4.2. Scalability and Network Independence

A fundamental property revealed by this analysis is the independence of the error bound from the total number of nodes

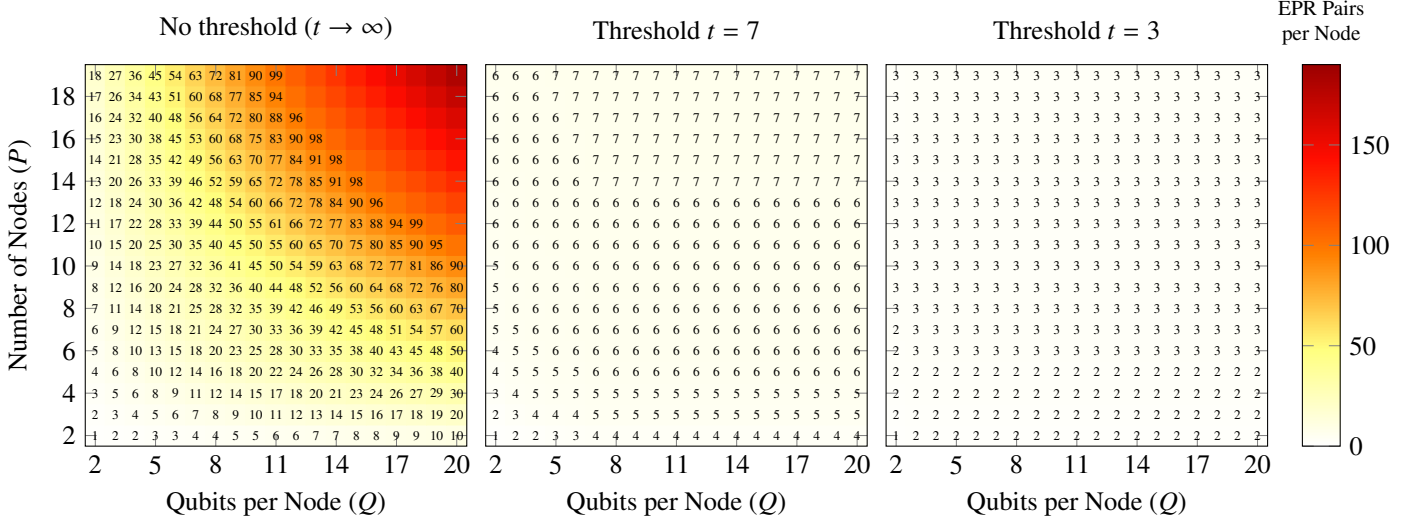


Figure 10: Density of entanglement resources, quantified as the number of EPR pairs generated *per computing node*, as a function of the local register size  $Q$  and the total number of nodes  $P$ . Note that **higher values correspond to increased communication overhead and resource consumption**. The leftmost panel (Unbounded) shows a linear increase in local resource demand with respect to  $P$ , implying a quadratic global complexity. The central ( $t = 7$ ) and rightmost ( $t = 3$ ) panels demonstrate how the pruning threshold effectively saturates this cost, rendering the resource consumption independent of the network size for sufficiently large distributed systems.

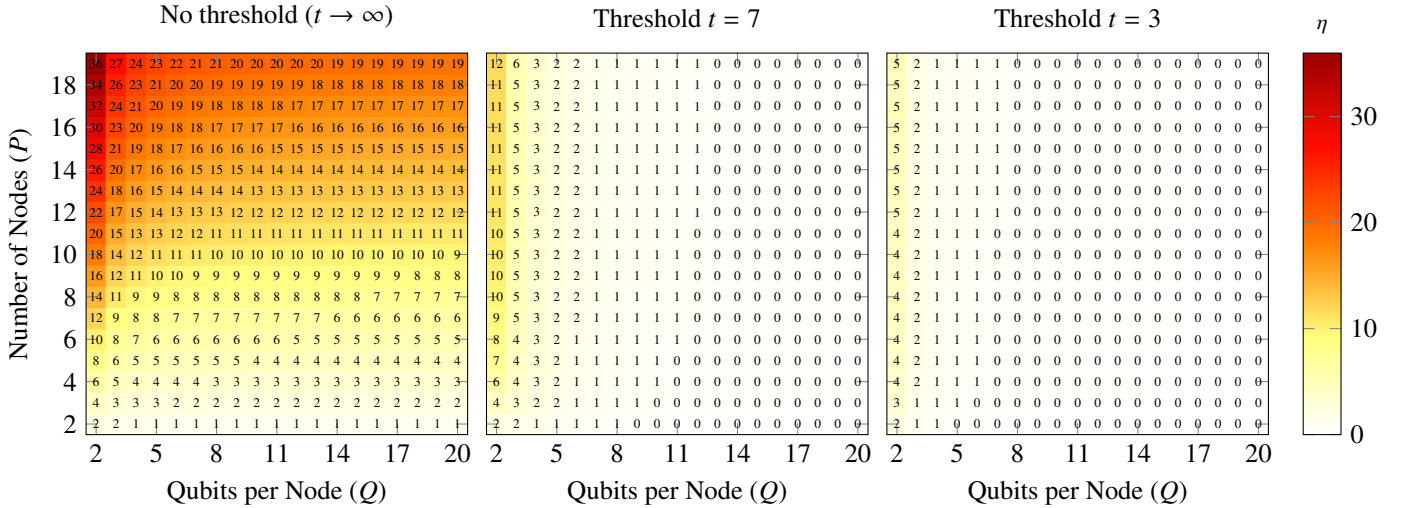


Figure 11: Evolution of the Coupling Ratio  $\eta$ , defined as the ratio between remote and local controlled-phase gates ( $\eta = N_{remote}/N_{local}$ ), as a function of the pruning threshold. Note that **higher values represent a higher dependency on inter-node communication**, which constitutes the primary bottleneck in distributed architectures. The plot demonstrates how the proposed pruning strategy successfully minimizes this ratio ( $\eta \rightarrow 0$ ), effectively decoupling the nodes and shifting the computational load towards efficient local processing.

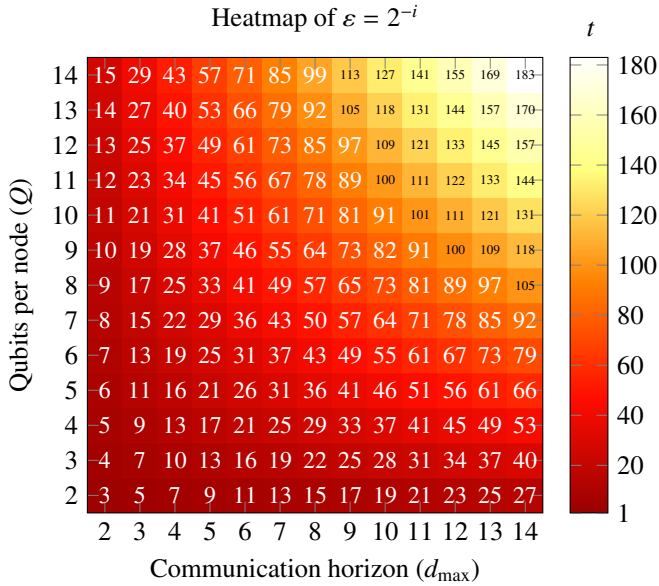


Figure 12: Impact of the communication horizon  $d_{\max}$  and local register size  $Q$  on the algorithmic accuracy. The values within the cells represent the **negated exponent  $i$**  of the theoretical error bound (such that  $\varepsilon \approx 2^{-i}$ ). Therefore, **higher values indicate lower errors and higher fidelity**. A rapid convergence is observed, showing that small horizons are sufficient to achieve high precision.

$P$ . The accuracy is determined solely by the local register size  $Q$  and the communication horizon  $d_{\max}$ . This implies that a horizon fixed at, for example,  $d_{\max} = 3$  ensures the same precision whether the network consists of  $P = 20$  nodes or scaled up to  $P = 100$  nodes.

This scalability is of paramount importance for the design of large-scale distributed quantum computers. It allows system architects to define a constant connectivity radius that guarantees a specific error tolerance  $\varepsilon$ , regardless of the global network size.

#### 4.5. Communication overhead

Figure 13 analyzes the Communication Overhead ratio ( $\gamma$ ) across different system sizes and pruning configurations. A crucial observation from these results is that the overhead factor remains relatively invariant with respect to the pruning threshold  $t$ .

This stability implies that the application of the threshold does not alter the fundamental architectural efficiency of the distributed protocol. The rationale lies in the fixed operational cost of the *Telegate* mechanism: each executed remote Controlled-Phase gate necessitates a specific, proportional set of auxiliary communication operations (Bell pair generation, entanglement swapping, and corrections). Therefore, when the pruning strategy removes a logical gate, it simultaneously eliminates the associated communication burden.

Consequently, while the *total count* of operations decreases drastically (as detailed in Section IV-C), the *ratio* between communication and computation tasks ( $\gamma$ ) remains stable. This confirms that the overhead is an intrinsic property of the chosen

quantum interconnect protocol and is not artificially inflated or distorted by the pruning approximation.

## 5. Discussion

The results presented in this work demonstrate that the communication aware optimization of the distributed iQFT significantly improves scalability without compromising algorithmic integrity. By restructuring the circuit to exploit the quadratic decay of controlled-phase rotation angles, we effectively transform a global, all-to-all interaction problem into a localized execution model. In this section, we analyze the implications of these findings regarding fidelity bounds, error convergence, and resource decoupling.

### 5.1. Fidelity and Theoretical Bounds

A critical observation from the fidelity analysis (Figure 9) is that the empirically simulated infidelity,  $1 - \mathcal{F}$ , is consistently lower than the theoretical upper bound derived in Eq. 22. The theoretical model assumes a worst-case scenario wherein every control qubit involved in a pruned interaction is in the state  $|1\rangle$ , thereby applying the maximum possible phase shift  $\theta_k$ . However, in a practical execution environment, the quantum register exists in a superposition of computational basis states. For any component of the wavefunction where the control qubit is  $|0\rangle$ , the controlled-phase gate acts as the identity  $\mathbb{I}$ , and its truncation introduces zero error. Consequently, the actual accumulated phase error is statistically lower than the sum of the absolute magnitudes of the discarded angles. This suggests that the proposed pruning thresholds are conservative, offering a safety margin where the realized algorithmic fidelity exceeds the strict design requirements.

### 5.2. Convergence of the Communication Horizon

The concept of the communication horizon,  $d_{\max}$ , emerges as a decisive parameter for distributed architecture design. As evidenced in Figure 12, the algorithmic error converges rapidly with respect to the interaction distance. For a local register size of  $Q = 4$ , limiting communications to a horizon of  $d_{\max} = 3$  nodes yields a theoretical error bound in the order of  $O(2^{-9})$ , which is negligible for most fault-tolerant applications. This rapid convergence validates  $d_{\max}$  as a sufficient metric to bound the network topology. It implies that for any target precision  $\varepsilon$ , the connectivity graph does not need to scale with the total number of nodes  $P$ . Instead, it effectively becomes a constant-degree graph depending only on  $Q$  and  $\varepsilon$ . This independence from  $P$  is a prerequisite for scalable distributed quantum computing, as it prevents the communication overhead from diverging as the system size increases.

### 5.3. Entanglement Resource Scaling

The impact of enforcing the communication horizon is most tangible in the consumption of EPR pairs. In the exact, unbounded implementation, the number of EPR pairs required per node grows linearly with the network size, leading to a

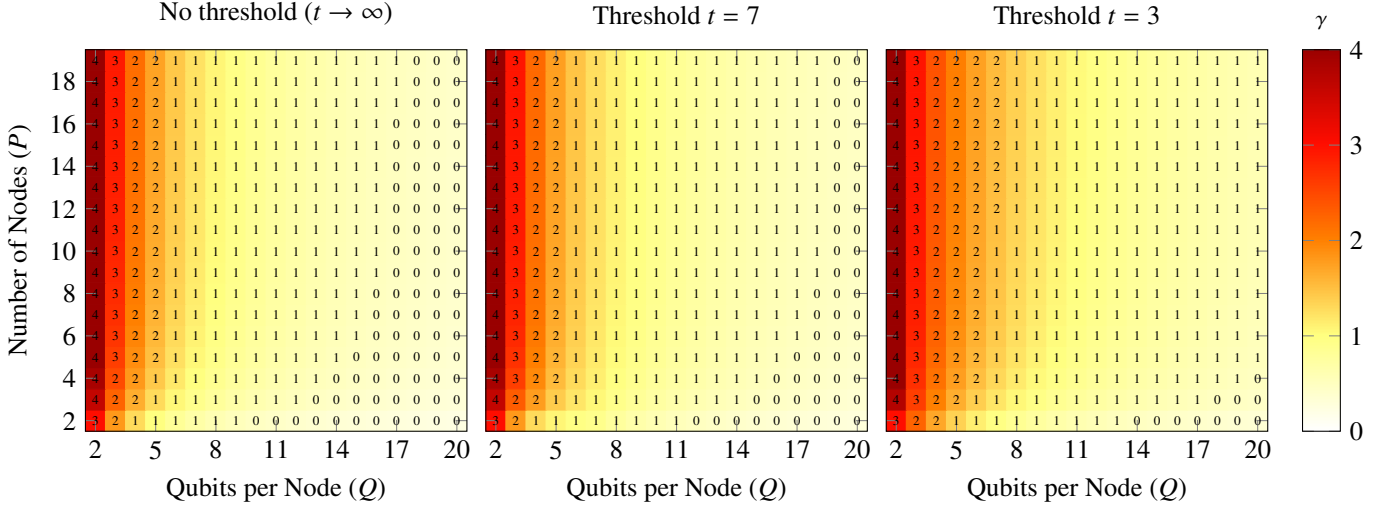


Figure 13: Global Communication Overhead  $\gamma$ , defined as the ratio between the number of auxiliary communication operations (entanglement generation, swapping, and corrections) and the logical computational gates ( $N_{\text{comm}}/N_{\text{comp}}$ ). This metric indicates the multiplicative factor by which the communication burden exceeds the useful processing work. Note that **higher values are detrimental**, representing a regime where the system execution is dominated by network maintenance rather than algorithmic progress.

quadratic aggregate complexity  $O(P^2)$ . This is observed in Figure 10 (left panel), where a system of  $P = 20$  nodes with  $Q = 20$  qubits necessitates  $\approx 180$  EPR pairs per node. Conversely, applying a pruning threshold of  $t = 7$  saturates this growth, capping the requirement at a maximum of approximately 7 EPR pairs per node (Figure 10, center panel), regardless of the network size. This transition from quadratic to linear global scaling (constant per node) indicates that the optimized distributed iQFT is resource-efficient, shifting the bottleneck from entanglement generation rates to local gate fidelities.

#### 5.4. Decoupling via the Coupling Ratio

Finally, the efficiency of the distributed decomposition is quantified by the Coupling Ratio,  $\eta = N_{CP}^{\text{remote}}/N_{CP}^{\text{local}}$  (Eq. 36). As illustrated in Figure 11, the standard algorithm exhibits a high dependency on remote operations, with  $\eta$  values reaching  $\approx 35$  for large systems, indicating that inter-node communication dominates the execution time. The application of the optimization strategy drastically suppresses this ratio. For thresholds  $t \leq 7$ ,  $\eta$  approaches asymptotic zero ( $\eta \rightarrow 0$ ). This reduction signifies a fundamental decoupling of the nodes: the computational workload is almost entirely confined to the local QPU, with inter-node links serving only for sparse, nearest-neighbor synchronization. This decoupling ensures that the latency of the quantum channel does not exponentially compound, thereby maintaining the coherence of the global state across the distributed processor.

## 6. Conclusions

In this work, we have presented a communication-aware optimization of the Inverse Quantum Fourier Transform (iQFT) designed specifically for distributed quantum architectures. By rigorously analyzing the geometric decay of the controlled-phase

rotation angles, we introduced a pruning strategy that transforms the algorithm's connectivity requirements from a global all-to-all topology to a bounded nearest-neighbor interaction model.

Our theoretical and empirical analyses demonstrate that establishing a communication horizon,  $d_{\text{max}}$ , allows for a drastic reduction in the consumption of entanglement resources. Specifically, we showed that the number of EPR pairs per node transitions from a linear scaling  $O(P)$  with respect to the network size to a constant saturation level  $O(1)$ , effectively making the resource overhead independent of the total number of nodes in the system. Furthermore, the analysis of the Coupling Ratio ( $\eta$ ) confirms that our method successfully decouples the processing nodes, reducing the dependency on high-latency inter-node links to near-zero values while maintaining algorithmic fidelity well within the theoretical error bounds derived.

Ultimately, this approach provides a scalable pathway for implementing large-scale Quantum Phase Estimation and other Fourier-based primitives on near-term networked quantum processors, offering a tunable trade-off between execution fidelity and communication bandwidth.

### 6.1. Future Work

While the current study utilized state-vector simulation to validate the theoretical error models and resource scaling exactitude, several key areas for future investigation. First, it would be valuable to extend the validation of this algorithm to specialized distributed quantum computing (DQC) simulators such as NetQMPI, CUNQA, or CUDA-Quantum. These platforms would allow for a more granular analysis of network-specific effects, including link latency, generation rates, and the impact of classical control delays on decoherence.

Additionally, future work should address the integration of this optimized iQFT schedule with quantum error correction

codes suitable for distributed environments, such as surface codes over noisy interconnects, to further suppress the effective error rates in the presence of realistic channel noise.

## Declaration of generative AI and AI-assisted technologies in the writing process

During the preparation of this work the authors used ChatGPT and Gemini in order to improve language and readability. After using this tool, the authors reviewed and edited the content as needed and take full responsibility for the content of the publication.

## Acknowledgments

This work was funded by European Union EuroHPC program with grant agreement 101194491 and by MICIU/AEI/10.13039/501100011033 with project number PCI2025-163229, the Agencia Estatal de Investigación (Spain) (PID2022-141623NB-I00), the Consellería de Cultura, Educación e Ordenación Universitaria Galician Research Center accreditation 2024–2027 ED431G-2023/04, and the European Regional Development Fund (ERDF).

## References

- [1] M. Caleffi, M. Amoretti, D. Ferrari, J. Illiano, et al., Distributed quantum computing: A survey, *Computer Networks* 254 (2024) 110672. doi:10.1016/J.COMNET.2024.110672. URL <https://www.sciencedirect.com/science/article/pii/S1389128624005048>
- [2] D. Barral, F. J. Cardama, G. Díaz-Camacho, D. Faílde, et al., Review of Distributed Quantum Computing: From single QPU to High Performance Quantum Computing, *Computer Science Review* 57 (2025) 100747. doi:10.1016/J.COSREV.2025.100747. URL <https://www.sciencedirect.com/science/article/pii/S1574013725000231>
- [3] H. Bluhm, L. R. Schreiber, Semiconductor spin qubits - A scalable platform for quantum computing?, *Proceedings - IEEE International Symposium on Circuits and Systems* 2019-May (2019). doi:10.1109/ISCAS.2019.8702477. URL <https://ieeexplore.ieee.org/abstract/document/8702477>
- [4] J. Preskill, Quantum Computing in the NISQ era and beyond, *Quantum* 2 (2018) 79. doi:10.22331/q-2018-08-06-79. URL <https://quantum-journal.org/papers/q-2018-08-06-79/>
- [5] J. Cacheiro, C. Sánchez, R. Rundle, G. B. Long, et al., QMIO: A tightly integrated hybrid HPCQC system, *Arxiv* 2505.19267 (5 2025). URL <https://arxiv.org/pdf/2505.19267>
- [6] S. Wehner, D. Elkouss, R. Hanson, Quantum internet: A vision for the road ahead, *Science* 362 (6412) (10 2018). doi:10.1126/SCIENCE.AAM9288. URL <https://doi/pdf/10.1126/science.aam9288?download=true>
- [7] D. Ferrari, A. S. Cacciapuoti, M. Amoretti, M. Caleffi, Compiler Design for Distributed Quantum Computing, *IEEE Transactions on Quantum Engineering* 2 (2021). doi:10.1109/TQE.2021.3053921. URL <https://ieeexplore.ieee.org/abstract/document/9334411>
- [8] J. Illiano, M. Caleffi, A. Manzalini, A. S. Cacciapuoti, Quantum Internet protocol stack: A comprehensive survey, *Computer Networks* 213 (2022) 109092. doi:10.1016/J.COMNET.2022.109092. URL <https://www.sciencedirect.com/science/article/pii/S1389128622002250>
- [9] P. Escofet, A. Das, S. B. Rached, S. Rodrigo, et al., On the Impact of Classical and Quantum Communication Networks Upon Modular Quantum Computing Architecture System Performance, 2025 IEEE International Conference on Quantum Computing and Engineering (QCE) (2025) 984–995doi:10.1109/QCE65121.2025.00110. URL <https://ieeexplore.ieee.org/abstract/document/11249763>
- [10] M. Palesi, E. Russo, G. Ascia, H. Rafique, et al., Assessing the Role of Communication in Modular Multi-Core Quantum Systems, *arXiv:2510.11053 1* (10 2025). URL <https://arxiv.org/pdf/2510.11053>
- [11] P. W. Shor, Algorithms for quantum computation: Discrete logarithms and factoring, *Proceedings - Annual IEEE Symposium on Foundations of Computer Science, FOCS (1994)* 124–134doi:10.1109/SFCS.1994.365700. URL <https://ieeexplore.ieee.org/document/365700>
- [12] D. Jiang, X. Liu, H. Song, H. Xie, An survey: Quantum Phase Estimation Algorithms, *IEEE Information Technology, Networking, Electronic and Automation Control Conference, ITNEC 2021 (2021)* 884–888doi:10.1109/ITNEC52019.2021.9587010. URL <https://ieeexplore.ieee.org/abstract/document/9587010>
- [13] C. G. Almudever, R. Wille, F. Sebastiano, N. Haider, et al., From Designing Quantum Processors to Large-Scale Quantum Computing Systems, *Proceedings -Design, Automation and Test in Europe, DATE (2024)*. doi:10.23919/DATE58400.2024.10546849. URL <https://ieeexplore.ieee.org/abstract/document/10546849>
- [14] D. Ferrari, S. Carretta, M. Amoretti, A Modular Quantum Compilation Framework for Distributed Quantum Computing, *IEEE Transactions on Quantum Engineering* 4 (2023). doi:10.1109/TQE.2023.3303935. URL <https://ieeexplore.ieee.org/abstract/document/10214316>
- [15] F. J. Cardama, J. Vázquez-Pérez, C. Piñeiro, T. F. Pena, et al., NetQIR: An extension of QIR for distributed quantum computing, *Future Generation Computer Systems* 174 (2026) 107989. doi:10.1016/J.FUTURE.2025.107989. URL <https://www.sciencedirect.com/science/article/pii/S0167739X25002845>
- [16] D. Coppersmith, An approximate fourier transform useful in quantum factoring, *arXiv:quant-ph/0201067* (2002). arXiv:quant-ph/0201067. URL <https://arxiv.org/abs/quant-ph/0201067>
- [17] J. I. Cirac, A. K. Ekert, S. F. Huelga, C. Macchiavello, Distributed quantum computation over noisy channels, *Physical Review A* 59 (6) (1999) 4249. doi:10.1103/PhysRevA.59.4249. URL <https://journals.aps.org/pr/abstract/10.1103/PhysRevA.59.4249>
- [18] F. V. Mendes, R. V. Ramos, Schemes for teleportation of quantum gates, *Quantum Information Processing* 2010 10:2 10 (2) (2010) 203–212. doi:10.1007/S11128-010-0189-7. URL <https://link.springer.com/article/10.1007/s11128-010-0189-7>
- [19] D. Main, P. Drmota, D. P. Nadlinger, E. M. Ainley, et al., Distributed quantum computing across an optical network link, *Nature* 2025 638:8050 638 (8050) (2025) 383–388. doi:10.1038/s41586-024-08404-x. URL <https://www.nature.com/articles/s41586-024-08404-x>
- [20] C. H. Bennett, G. Brassard, C. Crépeau, R. Jozsa, et al., Teleporting an unknown quantum state via dual classical and Einstein-Podolsky-Rosen channels, *Physical Review Letters* 70 (13) (1993) 1895. doi:10.1103/PhysRevLett.70.1895. URL <https://journals.aps.org/prl/abstract/10.1103/PhysRevLett.70.1895>
- [21] D. Gottesman, I. L. Chuang, Quantum Teleportation is a Universal Computational Primitive, *Nature* 402 (6760) (1999) 390–393. doi:10.1038/46503. URL <http://arxiv.org/abs/quant-ph/9908010http://dx.doi.org/10.1038/46503>
- [22] D. Gottesman, I. L. Chuang, Demonstrating the viability of universal quantum computation using teleportation and single-qubit operations, *Nature* 1999 402:6760 402 (6760) (1999) 390–393. doi:10.1038/46503. URL <https://www.nature.com/articles/46503>